A de novo strategy to develop NIR precipitating fluorochrome for long-term in situ cell membrane bioimaging

Ke Li[a], Yifan Lyu[a], Yan Huang[a], Shuai Xu[a], Hong-Wen Liu[a], Lanlan Chen[b], Tian-Bing Ren (任天兵)[a], Mengyi Xiong[a], Shuangyan Huan[a], Lin Yuan[a], Xiao-Bing Zhang (张晓兵)[a,1], and Weihong Tan[a]

[a]Molecular Science and Biomedicine Laboratory, State Key Laboratory of Chemo/Biosensing and Chemometrics, College of Chemistry and Chemical Engineering, Hunan University, 410082 Changsha, P. R. China; and [b]The Key Laboratory of Analysis and Detection Technology for Food Safety of the Ministry of Education, Fujian Provincial Key Laboratory of Analysis and Detection Technology for Food Safety, College of Chemistry, Fuzhou University, 350002 Fuzhou, P. R. China

Edited by Xin Zhang, Pennsylvania State University, University Park, PA, and accepted by Editorial Board Member Stephen J. Benkovic January 6, 2021 (received for review August 27, 2020)

Cell membrane–targeted bioimaging is a prerequisite for studying the roles of membrane-associated biomolecules in various physiological and pathological processes. However, long-term in situ bioimaging on the cell membrane with conventional fluorescent probes leads to diffusion into cells from the membrane surface. Therefore, we herein proposed a de novo strategy to construct an antidiffusion probe by integrating a fluorochrome characterized by strong hydrophobicity and low lipophilicity, with an enzyme substrate to meet this challenge. This precipitating fluorochrome HYPQ was designed by conjugating the traditionally strong hydrophobic solid-state fluorochrome 6-chloro–2-(2-hydroxyphenyl) quinazolin-4(3H)-one (HPQ) with a 2-(2-methyl–4H-chromen–4-ylidene) malononitrile group to obtain closer stacking to lower lipophilicity and elongate emission to the far-red to near-infrared wavelength. As proof-of-concept, the membrane-associated enzyme γ-glutamyltranspeptidase (GGT) was selected as a model enzyme to design the antidiffusion probe HYPQG. Then, benefiting from the precipitating and stable signal properties of HYPQ, in situ imaging of GGT on the membrane was successfully realized. Moreover, after HYPQG was activated by GGT, the fluorescence signal on the cell membrane remained unchanged, with incubation time even extending to 6 h, which is significant for in situ monitoring of enzymatic activity. In vivo testing subsequently showed that the tumor region could be accurately defined by this probe after long-term in situ imaging of tumor-bearing mice. The excellent performance of HYPQ indicates that it may be an ideal alternative for constructing universal antidiffusion fluorescent probes, potentially providing an efficient tool for accurate imaging-guided surgery in the future.

cell membrane–targeted bioimaging | precipitating fluorochrome | antidiffusion probe | long-term in situ imaging | in vivo bioimaging

The cell membrane is a glycerophospholipid bilayer that contains a variety of biomolecules, notably, lipids, carbohydrates, and proteins, which play indispensable roles in both pathological and physiological processes ranging from cell signaling to apoptosis and extracellular matrix processing (1–5). Therefore, bioimaging of membrane-associated biomolecules is significant for basic biological research and disease diagnosis (6, 7). Currently, several advanced methods and technologies have been developed for tracking biomolecules on the cell membrane surfaces, such as fluorescence imaging based on small-molecule probes, immunofluorescence assay, and flow cytometry (8). Among these methods, small-molecule probe-based fluorescence imaging plays an indispensable role in achieving in situ and real-time visualization of biomolecular activity on the cell membrane, requiring only rudimentary operation and highly sensitive display (9–11). Generally, current probes utilize amphiphilic molecules containing lipophilic alkyl chains for insertion into the plasma membrane and hydrophilic moieties to inhibit cellular internalization to detect biomolecules on the cell membrane (12–14). Nevertheless, properties of amphiphilicity, high mobility, and high biological activity of the cell membrane make conventional lipid-conjugated probes gradually diffuse into cell plasmas from the membrane surface after a certain period of time, thereby losing in situ information in long-term bioimaging of targets on the cell membrane and, finally, giving unreliable measurements (Scheme 1) (10, 15, 16). Alternatively, therefore, we have reported a solid-state fluorochrome-based strategy in order to design a fluorescent probe (HTPQA) for in situ bioimaging (17). Upon activation, it releases a hydrophobic fluorochrome that can precipitate at the reaction site to realize in situ imaging of alkaline phosphatase in living cells. Such a probe, however, is still not reliable enough for long-term bioimaging of cell membranes because of the obviously cellular internalization caused by the lipophilic property (17, 18). This calls for the development of an efficient antidiffusion probe to meet the long-term requirements for in situ bioimaging of live cell membranes.

To solve this problem, herein, we report the design and synthesis of a series of solid-state fluorochromes that work by an excited-state intramolecular proton transfer (ESIPT) mechanism.

Significance

Long-term in situ imaging of biomolecules on the cell membrane was significant for studying the physiological processes emitted from cell signaling and cell adhesion. Thus, to develop an efficient tool to realize in situ imaging membrane-associated biomolecules, we herein proposed a de novo strategy to construct an antidiffusion probe by integrating a fluorochrome (HYPQ) characterized by strong hydrophobicity and low lipophilicity, with an enzyme substrate. Then, benefiting from the antidiffusion property of the constructed probe HYPQG, long-term in situ imaging of membrane-associated enzyme GGT was successfully realized. This work may provide an efficient strategy for constructing universal antidiffusion fluorescent probes to realize long-term in situ bioimaging.

Author contributions: K.L., Y.L., S.H., L.Y., and X.-B.Z. designed research; K.L., Y.H., S.X., H.-W.L., L.C., T.-B.R., and M.X. performed research; K.L. and X.-B.Z. analyzed data; and K.L., L.Y., X.-B.Z., and W.T. wrote the paper.

The authors declare no competing interest.

This article is a PNAS Direct Submission. X.Z. is a guest editor invited by the Editorial Board.

Published under the PNAS license.

[1]To whom correspondence may be addressed. Email: xbzhang@hnu.edu.cn.

This article contains supporting information online at https://www.pnas.org/lookup/suppl/doi:10.1073/pnas.2018033118/-/DCSupplemental.

Published February 18, 2021.

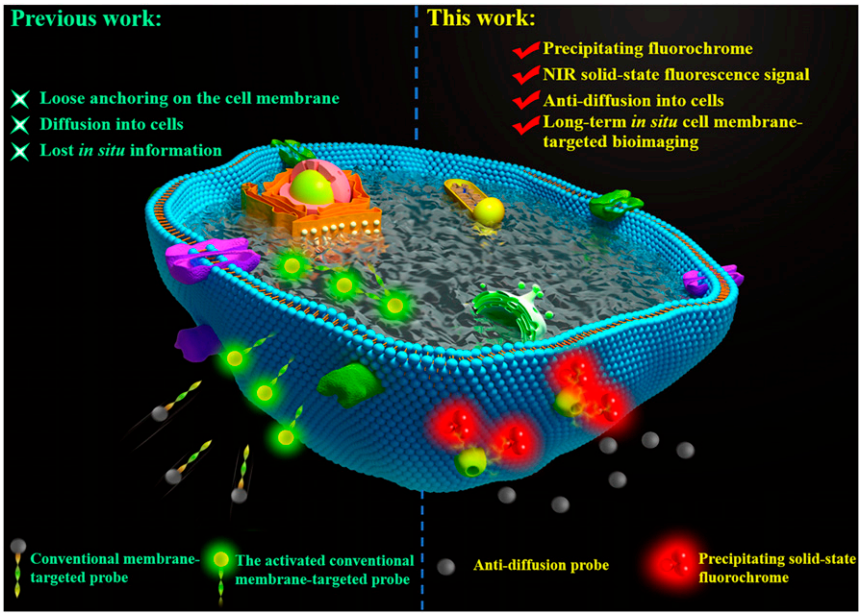

Scheme 1. Schematic diagram illustrates the difference between conventional cell membrane-targeted bioimaging probes and our de novo anti-diffusion bioimaging probe. Traditional membrane-associated probes easily diffuse into cells, while the anti-diffusion probe releases a strong hydrophobicity and low lipophilicity fluorochrome that precipitates at the reaction sites in a manner that inhibits diffusion into the cell, hence, realizes long-term in situ cell membrane-targeted bioimaging.

From these candidate fluorophores, we screened out a type of near-infrared (NIR) precipitating solid-state fluorochrome termed HYPQ. Its tunable fluorescence and insolubility are closely related to an internal hydrogen bond between the phenolic hydrogen and the imine nitrogen. Based on this concept, we proposed a de novo strategy to realize long-term in situ bioimaging on the cell membrane by introducing HYPQ to construct an antidiffusion membrane probe (Scheme 1). As proof-of-concept, the enzyme-responsive probe HYPQG was developed, targeting membrane-associated enzyme γ-glutamyl transpeptidase (GGT) as a model enzyme, because of its vital role in the growth and migration of human malignancies, especially in epithelial cancers (19–23). HYPQG is nonfluorescent with good hydrophilicity by inhibition of ESIPT which masks the phenolic hydroxyl by the water-soluble group of γ-glutamyl. Upon specific reaction with GGT on the cell membrane, the free fluorophore HYPQ is released and precipitates at the reaction sites, preventing further diffusion into cells, thereby achieving long-term in situ imaging of GGT on the living cell surface and in the tumor region. Since GGT and other membrane-associated enzymes have been identified as biomarkers for various cancers, our research might also provide an efficient tool for accurate imaging-guided surgical resection. This is a report of such an antidiffusion fluorescent probe for long-term in situ enzyme activity imaging on live cell membranes.

Results and Discussion

Design and Synthesis of NIR Precipitating Fluorochrome. We previously demonstrated that the solid-state fluorescent probes HTPQA and HPQF could release a hydrophobic fluorochrome for in situ imaging of biomarkers in living cells (17, 18). However, it is still difficult to apply them to long-term in situ bioimaging on cell membranes owing to their lipophilicity. Besides, the limited emission wavelength hindered the application of these solid-state fluorochromes in vivo. Therefore, we set about verify.designing a strong hydrophobicity and low-lipophilicity fluorochrome based on the traditional solid-state fluorophore HPQ with emission wavelength extending to the far-red to NIR region (Scheme 2). To obtain a useful NIR precipitating HPQ-analog solid-state fluorochrome, there are three vital principles needed to be considered: (1) redshift the emission wavelength to the NIR region (≥ 650 nm); (2) decreasing the lipophilicity, meanwhile, keeping strong hydrophobicity; (3) keeping smaller steric hindrance to develop enzyme-activatable probes. As is known, the combination of donor–acceptor interaction and π-conjugation may efficiently redshift the fluorescence of fluorochrome (24, 25). Meanwhile, the good planarity could promote intermolecular π−π stacking interaction (26, 27), thereby decreasing the solubility and realizing antidiffusion imaging.

As previously reported, the replacement of hydrogen at the R1 position with chlorine-induced bathochromic shifts in HPQ (28, 29). Therefore, we tried creating a red-shifted solid-state fluorophore, termed HPQ1, in which chlorine was replaced with a 4-(trifluoromethyl) styrene residue. However, only limited bathochromic shift (20 nm) was achieved, as observed in *SI Appendix*, Table S1. This phenomenon could be attributed to π-conjugation at the R1 position which cannot narrow the energy gap of HPQ1 efficiently, as also verified by the density functional theory (DFT) calculation (*SI Appendix*, Fig. S1*A*) (30). Therefore, we next attempted to alter the substituted groups on the parapositioned phenolic hydroxyl. For HPQ2, an electron-donating diethylamino group was introduced at this position, while quenched solid-state fluorescence occurred (*SI Appendix*, Fig. S2 and Table S1), probably because of the intramolecular photoinduced electron transfer (IPET) or twisted intramolecular charge transfer mechanism (31). Time-dependent DFT calculation suggested that the electron was mainly distributed in the dialkylamino donor substituents of the highest occupied molecular orbital of HPQ2 compared with HPQ-H (*SI Appendix*, Fig. S1). The analog (HPQ-N) of HPQ2 was synthesized by rigidifying dialkylamino donor moieties to further confirm that the reason of quenched fluorescence mainly resulted from IPET mechanism (*SI Appendix*, Fig. S2) (32). In contrast, the electron-withdrawing unit, e.g., N-methylpyridinium, on this position exhibited a long-emission wavelength (HPQ3: λ_{em} = 590 nm), although its lipophilicity did not change (*SI Appendix*, Fig. S3*B*). Thus, it seemed to be a rational design strategy to obtain a red-shifted solid-state

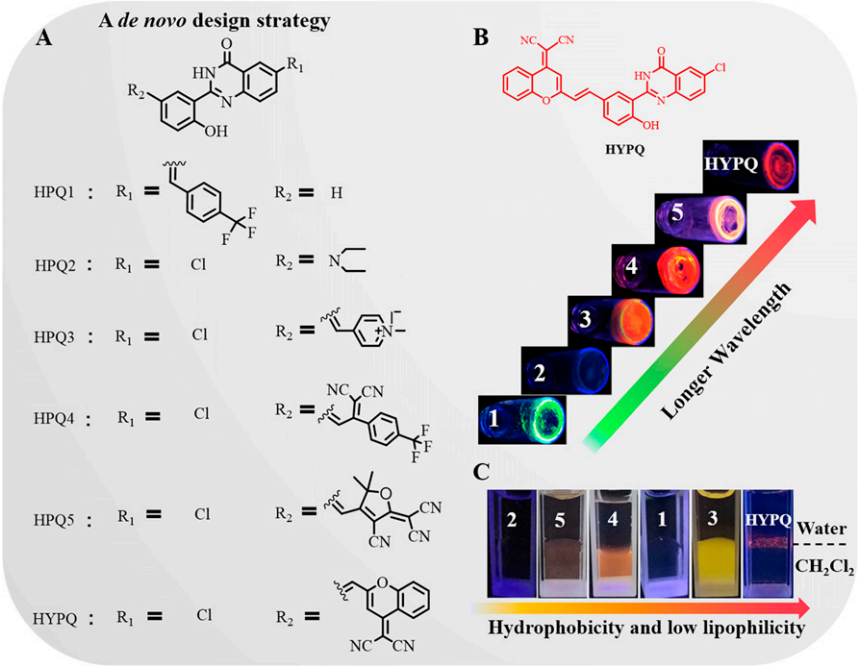

Scheme 2. The design of hydrophobicity and low lipophilicity NIR solid-state fluorochrome. (A) A de novo design strategy for developing solid-state fluorophores. (B) Solid-state fluorescent photographs of those fluorophores in the powder samples. (C) Diffusion experiments were conducted at the interface between water and dichloromethane (amphiphilic environment). All fluorescent photos were obtained under UV lamp excitation at 365 nm.

fluorochrome by introducing an electron-withdrawing moiety on the parapositioned phenolic hydroxyl. Using this strategy, HPQ4 and HPQ5 were then designed by introducing different electron-withdrawing groups. These resultant solid-state fluorochromes showed obvious bathochromic shifts in emission spectrum (HPQ4: λ_{em} = 625 nm, HPQ5: λ_{em} = 636 nm) (*SI Appendix*, Fig. S3*C*), but were still lipophilic (*SI Appendix*, Fig. S3*B*). The crystal structures of HPQ and HPQ4 were unambiguously confirmed by single crystal X-ray analysis, as shown in *SI Appendix*, Fig. S4. Crystal packing of HPQ and HPQ4 suggested existence of strong OH···N intramolecular (HPQ: 1.831 Å, HPQ4: 1.863 Å) H-bonding and NH···O intermolecular H-bonding (HPQ: 2.101 Å, HPQ4: 2.042/1.960 Å) interaction in crystal lattices. Additionally, the intermolecular interactions led to the formation of HPQ or HPQ4 dimer which was further interconnected through π–π interactions in crystal lattices. The weakened planarity of HPQ4 resulted from the twist deformation of substituted groups on the parapositioned phenolic hydroxyl (*SI Appendix*, Table S2), which caused larger intermolecular distances between the HPQ4 dimers (2.941 to 3.354 Å) (*SI Appendix*, Fig. S4*B*). It is well known that the amphiphilicity of the cell membrane causes liposoluble fluorochromes to diffuse into cells from the membrane (15). The lipophilicity of these solid-state fluorophores might be ascribed to their loose aggregation in the liposoluble environment because the substituted groups weakened the planarity of precursor structure so as to suppress the close stacking of molecules (*SI Appendix*, Tables S2, S3, and S5) (33). The 2-(2-methyl–4H-chromen–4-ylidene) malononitrile was reported to be a strong electron-withdrawing unit and possessed good planarity with facile aggregation (34–36). Therefore, we attempted to integrate it into our HPQ structure to design a solid-state fluorochrome HYPQ, to obtain closer stacking that would afford lower lipophilicity and, meanwhile, elongate the emission wavelength.

As expected, the solid-state fluorescence emission of HYPQ was extended to the NIR region (650 nm) by introducing this strong electron-withdrawing group (*SI Appendix*, Table S1). Lipophilicity of HYPQ, HPQ, and HTPQ was then studied in dichloromethane (CH_2Cl_2), which is known as a good solvent and could provide a liposoluble environment (37, 38). As shown in *SI Appendix*, Fig. S6, 10 μM HPQ and HTPQ showed no obvious solid-state fluorescence in dichloromethane because the fluorochromes were completely dissolved. On the contrary, 10 μM HYPQ was insoluble in dichloromethane and thus could be observed as red solid-state fluorescence under ultraviolet (UV) lamp excitation at 365 nm (*SI Appendix*, Fig. S6). It was further confirmed from the change of absorbance spectra of these solid-state fluorochrome in phosphate-buffered saline (PBS) or dichloromethane solutions before (black lines) and after (red lines) filtration (Fig. 1 *A* and *B* and *SI Appendix*, Fig. S3). Besides, the solubilities of HPQ, HTPQ, HPQ1, HPQ2, HPQ3, HPQ4, HPQ5, and HYPQ in dimethyl sulfoxide (DMSO) solutions were also measured by using UV absorbance. Among these solid-state fluorochromes, the solubility of HYPQ was the worst, and the dissolved concentration was less than 1 μM even in DMSO and dimethyl formamide (*SI Appendix*, Fig. S7). Moreover, we measured their melting points, as well as optimized the structures of these solid-state fluorophores to further explain the relationship between the properties and molecule structures. As shown in *SI Appendix*, Fig. S7 and Tables S2, S3, and S5, the melting point and solubility of these solid-state fluorophores presented some important relevance with the twisted angle between the substituted groups and HPQ structure. The more tightly intermolecular π–π stacking interaction may result from the better planarity of solid-state fluorophores, thereby decreasing the solvation in medium and raising the melting point (*SI Appendix*, Table S5). All these experimental results suggested that HYPQ had the strongest hydrophobicity and lowest lipophilicity among the various solid-state fluorophores.

The antidiffusion property of HYPQ was further investigated and compared with a water-soluble fluorochrome, 7-Amino–4-methylcoumarin (AMC), and a liposoluble fluorochrome, 2-(4-aminostyryl)–4H-chromen–4-ylidene malononitrile (DCM-NH_2),

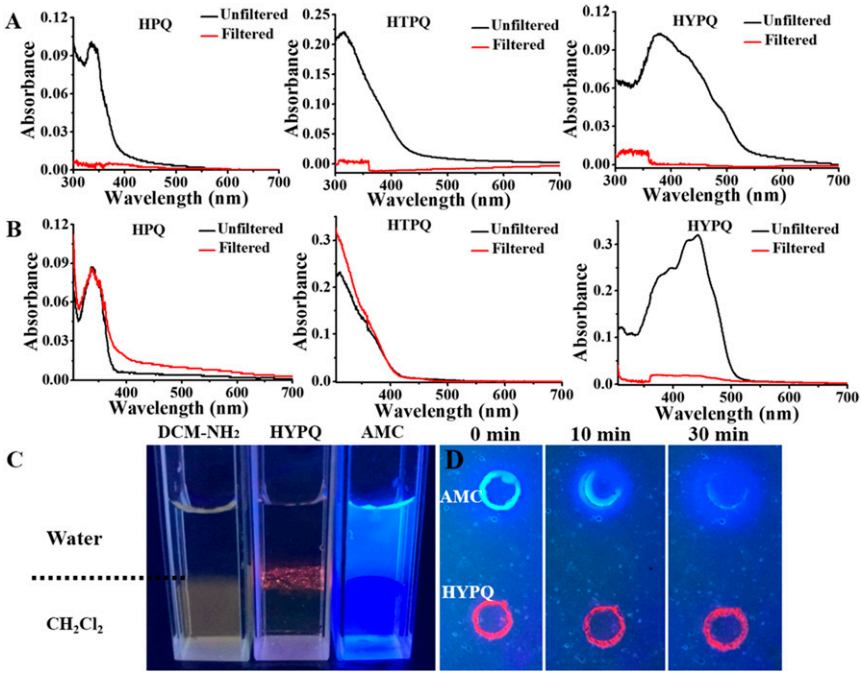

Fig. 1. The comparison of solubility of HPQ, HTPQ, HYPQ, AMC (a water-soluble fluorochrome), and DCM-NH_2 (a liposoluble fluorochrome). The absorbance spectra of HPQ, HTPQ, and HYPQ (10 μM) in PBS containing 1% DMSO and 10% glycerol (*A*) and in dichloromethane (*B*). The black and red lines indicate the absorbance spectra intensity of these compounds before and after filtration. (*C*) Diffusion experiments of DCM-NH_2, HYPQ, and AMC were performed at the interface between water and dichloromethane (amphiphilic environment). (*D*) Agarose gels containing HYPQ and AMC were immersed in PBS (pH = 7.4), and then real-time images were obtained every 10 min for a total of 30 min. HYPQ showed good antidiffusion ability, while AMC diffused rapidly within 30 min. All the fluorescent photos were conducted under UV lamp excitation at 365 nm.

by adding them into the mixture of water and dichloromethane. One can easily see that only HYPQ could stay at the interface of water/dichloromethane, indicating that it neither dissolved in dichloromethane nor in water (Fig. 1*C*). After HYPQ and AMC were, respectively, spotted on agarose gels and immersed in PBS (pH = 7.4) for 30 min, HYPQ possessed good antidiffusion ability compared with AMC (Fig. 1*D*).

Meanwhile, the chemical stability of HYPQ was examined in the presence of various reactive oxygen species (O_2^-, H_2O_2, ClO^-) and reactive sulfur species (S^{2-}, S_2^{2-}, SO_3^{2-}). Also, the photostability of HYPQ was compared with traditional cyanine dyes (Cy5) under illumination with white light. As shown in *SI Appendix*, Fig. S9, HYPQ exhibited good chemical stability and photostability. The other photophysical characterizations of HYPQ were shown in *SI Appendix*, Fig. S8 and Table S6. Therefore, we screened out an NIR precipitating fluorochrome with good chemical stability and photostability, which would be favorable for the construction of de novo universal antidiffusion fluorescent probes to realize long-term in situ cell membrane–targeted bioimaging.

Design and Synthesis of an Antidiffusion Fluorescent Probe. GGT is a plasma membrane-bound ectoenzyme that initiates the degradation of extracellular glutathione (GSH) into glycine and cysteine (19–22). GGT-mediated hydrolysis of extracellular GSH may confer a growth advantage for tumor cells because this process provides a way for cells to recover cysteine (23, 39). However, it is still a challenge for traditional methods to realize in situ imaging of GGT activity on the cell membrane (40–48). Nonetheless, the vital role of GGT in tumor progression and invasion calls for the development of an effective tool to visualize in situ information on the cell membrane.

Taking advantage of our precipitating solid-state fluorochrome HYPQ, the NIR antidiffusion fluorescent probe HYPQG was developed by introducing a specific recognition group γ-glutamyl into HYPQ through a self-immolative linker (Fig. 2*A*). The self-immolative linker in the probe not only minimizes steric hindrance at the reaction sites, but also improves the stability of HYPQG (28, 29). Control probes HPQG and HTPQG were also synthesized using the same design strategy. For better comparison, control probes (AMCG, DCMG, Cv-Glu, Bcy-GGT, and Np-Glu) with traditional lipophilic fluorochrome and hydrophilic fluorochrome were also prepared by introducing the specific recognition group (*SI Appendix*, Scheme S3). All synthetic routes (*SI Appendix*, Schemes S1 and S4), NMR, and mass spectra are illustrated in *SI Appendix*, Figs. S37 and S83.

Fluorescent Response Properties of Probe HYPQG to GGT. The absorption spectra of HYPQ and HYPQG are shown in Fig. 2*B*. The fluorescence intensity was dramatically increased, with a maximum wavelength at 650 nm, owing to GGT-mediated formation of HYPQ (Fig. 2*C*). These results were also proved by matrix-assisted laser desorption/ionization time of flight mass spectrometry spectrum analysis (*SI Appendix*, Fig. S10). To further confirm the specific hydrolysis of HYPQG by GGT, 6-Diazo–5-oxo–L-norleucine (DON, an inhibitor of GGT) was applied to investigate the response of HYPQG to the activity of GGT. As shown in *SI Appendix*, Fig. S11*A*, initial incubation of GGT with different concentrations of DON followed by treatment with HYPQG led to a larger decrease in fluorescence signal. These results proved that the increased fluorescence signal of HYPQG was truly caused by GGT-induced hydrolysis. Moreover, the time-course response of HYPQG to GGT was studied by measuring fluorescence intensity at 650 nm in real time. The fluorescence signal gradually reached a plateau in 30 min, with different concentrations of GGT and 5 μM HYPQG, which suggested that the probe was hydrolyzed rapidly by GGT (*SI Appendix*, Fig. S11*B*). In addition, good linear

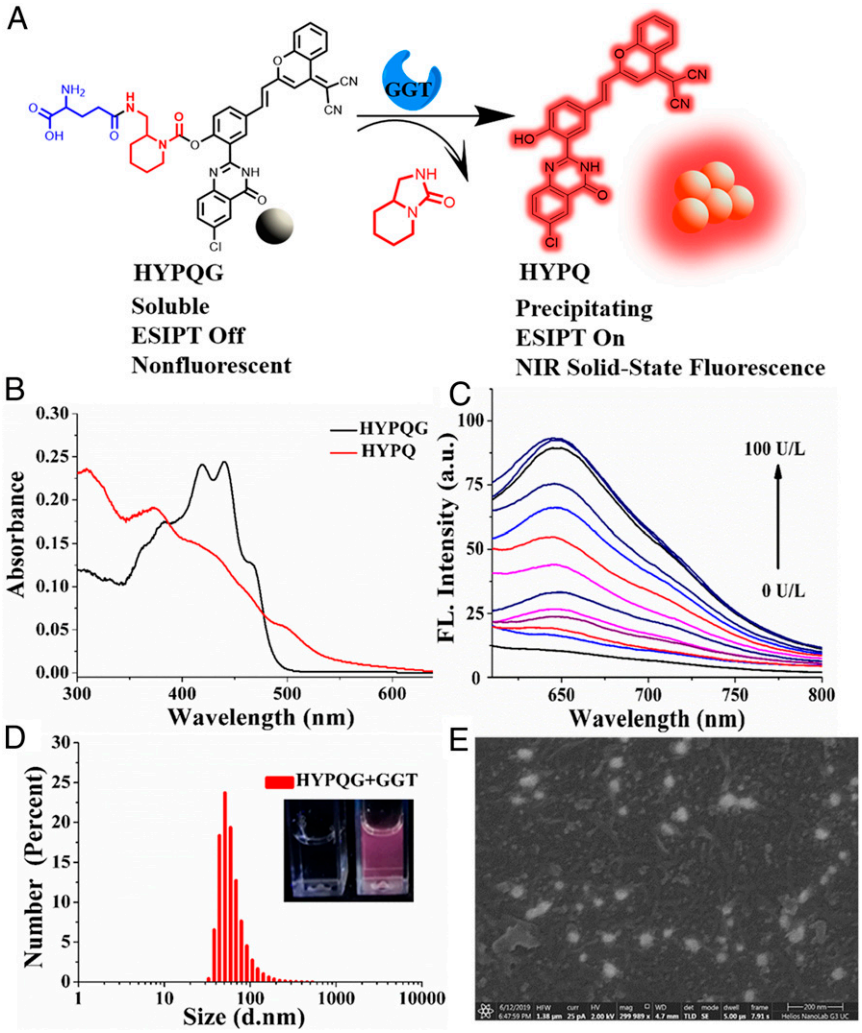

Fig. 2. The chemical structure and photophysical properties of HYPQG. (*A*) The response mechanism of HYPQG with GGT that shows turn-on NIR solid-state fluorescence. (*B*) UV-Vis absorption spectra of HYPQG (10 μM) in DMSO and HYPQ (10 μM) in glycerol: PBS = 1:1. (*C*) Fluorescence emission spectra of HYPQG (5 μM) with increasing concentration of GGT (0, 1, 3, 5, 10, 15, 20, 30, 40, 60, 80, 90, and 100 U/L). $\lambda_{ex/em}$ = 450/650 nm. (*D*) Particle size distributions of HYPQG (10 μM) after reaction with GGT (150 U/L). (*Inset*) Photos of HYPQG (10 μM) before (*Left*) and after (*Right*) reaction with GGT (150 U/L) under UV lamp at 365-nm excitation. d, diameter. (*E*) SEM photos of HYPQG after reaction with GGT. HFW, horizontal field width; HV, high voltage. (Scale bar, 200 nm.)

relationship occurred between fluorescent intensity and the increasing GGT level (1–30 U/L), and a detection limit for GGT of 0.83 U/L was calculated (*SI Appendix*, Fig. S12*A*). The Michaelis constant (K_m) of the probe with GGT was determined as 8.54 μM by using the Lineweaver–Burk plot, which indicated that the probe had strong affinity with GGT (*SI Appendix*, Fig. S13). The effect of acidity on the response of the probe is shown in *SI Appendix*, Fig. S12*B*. It was found that maximum fluorescence enhancement could be achieved in neutral media of about pH 7, which suggested that the probe was suitable for imaging GGT under physiological conditions. In addition, the selectivity of HYPQG for GGT in the presence of various reactive species was also investigated, which indicated that HYPQG displayed high specificity for GGT (*SI Appendix*, Fig. S14). The precipitated form, as converted by GGT, was also characterized by dynamic light scattering, scanning electron microscope (SEM), and transmission electron microscope, respectively (Fig. 2 *D* and *E* and *SI Appendix*, Fig. S15). At the same time, the fluorescence response properties of the control probes to GGT were studied. As shown in *SI Appendix*, Fig. S17, no fluorescence was observed in HTPQG solution after incubation with GGT because of the large steric hindrance of HTPQ. The docking simulation results showed that the reaction sites of probe HYPQG and AMCG had obvious hydrogen bond interactions with the active catalytic site of GGT (*SI Appendix*, Fig. S16*A*) (49, 50). However, the HTPQG failed to dock into the ligand-binding pocket of GGT to form hydrogen bond interactions due to the large steric hindrance, which further caused the bad reactivity (*SI Appendix*, Fig. S16*A*). All other control probes exhibited good fluorescent response to GGT (*SI Appendix*, Figs. S18–S20).

In Situ Imaging of Endogenous GGT on Cell Membranes. First, the cytotoxicity of HYPQG was evaluated by 3-(4,5-dimethylthiazol-2-yl)-5-(3-carboxymethoxyphenyl)-2-(4-sulfophenyl)-2H-tetrazolium assay. As shown in *SI Appendix*, Fig. S22*C*, the viability of A2780, OVCAR3, NIH 3T3, and HepG2 cells remained unchanged, with probe concentration ranging from 2 to 30 μM, indicating that HYPQG possessed good biocompatibility. In addition, we also prepared the photoactivatable HYPQ for further investigating the cytotoxicity of HYPQ in living cells, and the results showed that HYPQ had low cytotoxicity even at a high dose (30 μM) (*SI Appendix*, Figs. S21 and S22 *A* and *D*). Human

ovarian cancer cell line A2780 expresses a high level of GGT on the cell membrane (40). Probes HYPQG, AMCG, DCMG, Cv-Glu, Bcy-GGT, and Np-Glu were, respectively, incubated with A2780 cells for 40 min and then cultured with Memb-Tracker Green for 10 min, before fluorescence imaging. As shown in Fig. 3*A*, the overlap coefficient indicated that only HYPQG could achieve in situ imaging of GGT on the A2780 cell surface. Three-dimensional reconstructed and Z-stack images of A2780 cells were further conducted to confirm the colocalization experiments (Fig. 3*B* and *SI Appendix*, Fig. S23). Meanwhile, traditional solid-state fluorophores HPQ and HTPQ were designed as probes to image endogenous GGT in A2780 cells. However, neither HPQG nor HTPQG could achieve in situ imaging of GGT in A2780 cells owing to the lipophilic character of HPQ and large steric hindrance of HTPQ (*SI Appendix*, Fig. S24). The colocalization experiments were also performed by using commercially available Mito-Tracker Blue, Lyso-Tracker Blue, and Hoechst33258, respectively (*SI Appendix*, Fig. S25), which further confirmed that the released fluorophore HYPQ from HYPQG only precipitates on the cell membrane. In addition, both confocal laser scanning microscope (CLSM) (*SI Appendix*, Figs. S26 and S27) and flow cytometry results (*SI Appendix*, Fig. S28) confirmed that the fluorescence signals from the probes were all largely decreased in A2780 cells after treatment with DON, suggesting that the enhancement of fluorescence was indeed triggered by GGT on the cell membrane. All experimental results showed that both lipophilic and hydrophilic fluorochromes can easily diffuse into cells from the membrane surface, whereas the HYPQ did not, thereby realizing in situ imaging of GGT on the cell membrane.

In situ imaging ability was mainly based on the antidiffusion ability and stable signal of a probe. Therefore, the antidiffusion performance of HYPQG was further investigated by comparison with the commercially available GGT probe AMCG. As shown in *SI Appendix*, Fig. S29, after HYPQG and AMCG were, respectively, cultured with A2780 cells, real-time images were collected every 10 min, for a total of 90 min. The AMCG probe released the hydrophilic fluorochrome AMC after reacting with GGT and was then transported into A2780 cells. The fluorescence signal was quickly lost during the course of diffusion. In contrast, the fluorescence signal of HYPQ remained unchanged for a long time, demonstrating that HYPQG was an antidiffusion fluorescent probe. Next, after the cells were incubated with HYPQG and Memb-Tracker Red, respectively, real-time fluorescence scanning was carried out. As shown in *SI Appendix*, Fig. S30, the fluorescence signal of HYPQ remained unchanged, while the Memb-Tracker Red signal quickly decreased after scanning for 15 min. These results proved that HYPQ exhibited excellent antidiffusion and stable signal properties, both suitable for in situ imaging of GGT on the cell membrane.

Long-term in situ imaging of biomolecules on the cell membrane was significant for real-time monitoring of the pathological and physiological processes emitted from cell signaling, cell adhesion, and extracellular matrix processing (3). Considering the excellent properties of HYPQ, we next investigated the long-term imaging ability of HYPQG on the cell membrane. First, the fluorescence signal on the cell membrane of A2780 cells was gradually increased and reached a plateau after incubation with HYPQG for 30 min (*SI Appendix*, Fig. S31). When the fluorescence signal intensity became stable, real-time imaging for the same region of A2780 cells was obtained every 10 min, for a total of 240 min (*SI Appendix*, Fig. S32). To avoid the influence of photobleaching and morphological change of cells during long-term imaging, we also investigated the long-term imaging ability

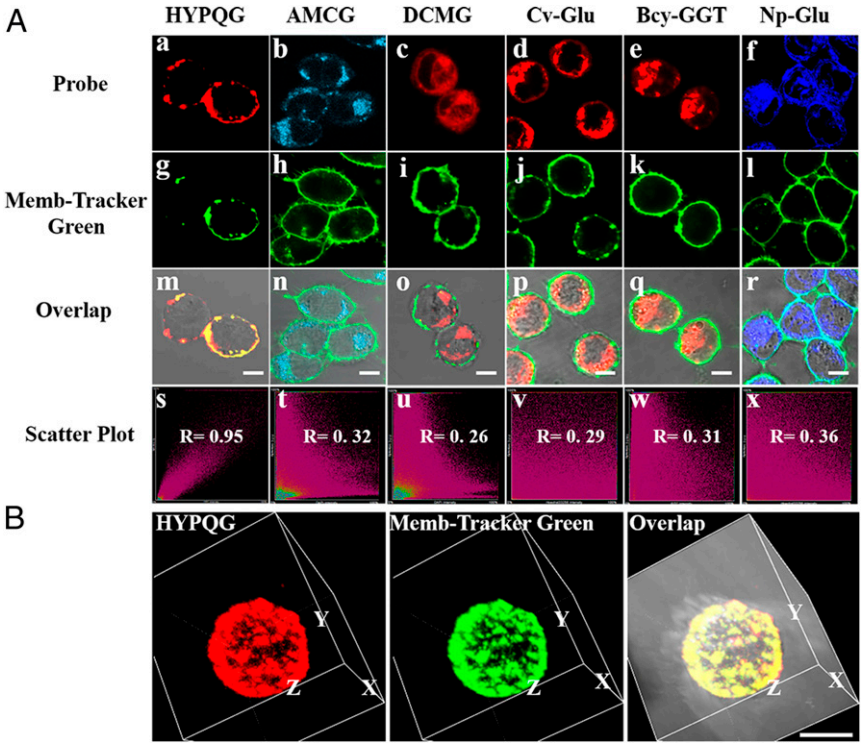

Fig. 3. In situ imaging of endogenous GGT on the cell membrane with HYPQG and the other five traditional GGT probes. (*A*) A2780 cells were pretreated with 5 μM HYPQG (a), 5 μM AMCG (b), 5 μM DCMG (c), 5 μM Cv-Glu (d), 5 μM Bcy-GGT (e), or 5 μM Np-Glu (f) for 40 min, respectively, and then cultured with 5 μM Memb-Tracker Green for 10 min (g–l), followed by fluorescence imaging. All overlapping images (m–r) and colocalization images (s–x) of the probe and Memb-Tracker Green, respectively. (*B*) Three-dimensional reconstructed images after incubating A2780 cells with HYPQG and Memb-Tracker Green. HYPQG: λ_{ex} = 488 nm, λ_{em} = 584–676 nm; AMCG: λ_{ex} = 405 nm, λ_{em} = 425–475 nm; DCMG: λ_{ex} = 488 nm, λ_{em} = 663–738 nm; Cv-Glu: λ_{ex} = 560 nm, λ_{em} = 584–676 nm; Bcy-GGT: λ_{ex} = 640 nm, λ_{em} = 663–738 nm; Np-Glu: λ_{ex} = 405 nm, λ_{em} = 425–475 nm; Memb-Tracker Green: λ_{ex} = 488 nm, λ_{em} = 500–550 nm. (Scale bar, 20 μm.)

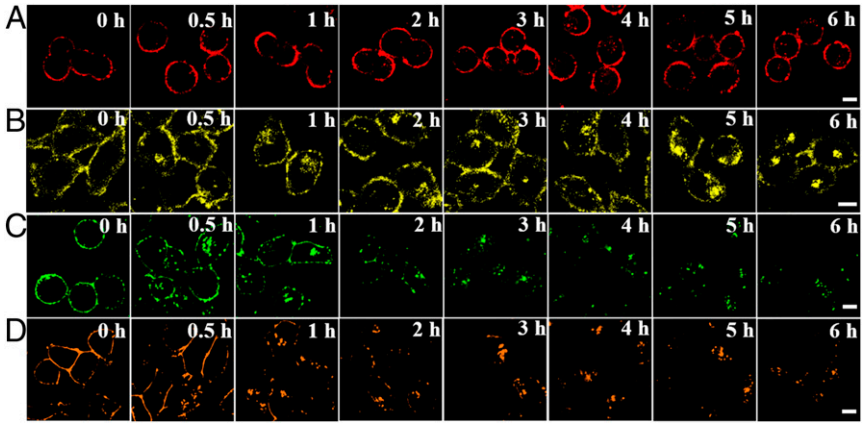

Fig. 4. The long-term in situ images of HYPQG, HTPQA, Memb-Tracker Green, and Memb-Tracker Red in live cells. Cells were incubated with HYPQG (*A*), HTPQA (*B*), Memb-Tracker Green (*C*), and Memb-Tracker Red (*D*) for different times; then fluorescence imaging was carried out. All "0 h" fluorescence images were times when the fluorescence signal reached a plateau for each probe, thus ensuring that the long-term imaging experiments were performed under the same conditions. (Scale bar, 20 μm.)

for the different regions of A2780 cells. As shown in Fig. 4*A*, the fluorescence signal on the cell surface remained unchanged, and the incubation time was even extended to 6 h. Because of the lipophilic properties of the traditional solid-state fluorochrome HTPQ, the signal on the cell membrane was also gradually diffused into cells after HepG2 cells were cultured with the HTPQA probe for 3 h (Fig. 4*B*). In addition, we investigated the long-term imaging ability of commercially available membrane-imaging probes (Memb-Tracker Green and Memb-Tracker Red). As illustrated in Fig. 4 *C* and *D*, the membrane-imaging signal of Memb-Tracker Red was more easily diffused into cells than that of Memb-Tracker Green, which may be the result of the better lipophilicity of the former over that of the latter. All in all, long-term in situ bioimaging on the cell membrane was successfully realized, owing to the outstanding antidiffusion properties of HYPQ.

Next, HYPQG was applied for in situ imaging of GGT on the cell membrane of three kinds of cancer cells with different

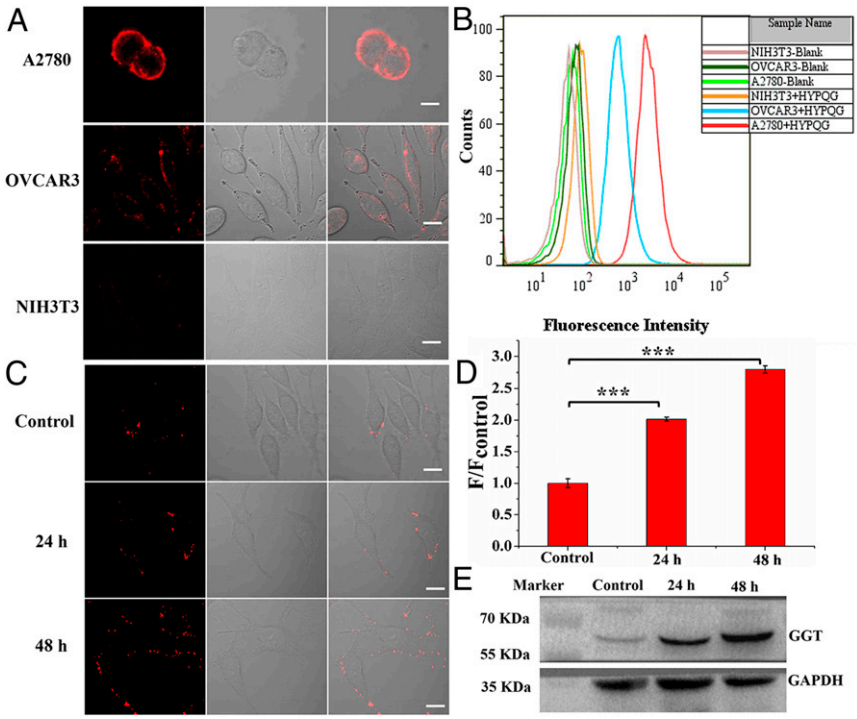

Fig. 5. In situ imaging of different expression levels of GGT on the membrane of cancer cells. (*A*) A2780, OVCAR3, and NIH 3T3 were incubated with HYPQG (5 μM) for 40 min at 37 °C, respectively, followed by fluorescence imaging. (*B*) Flow cytometric analysis after incubation with HYPQG in A2780, OVCAR3, and NIH 3T3 cancer cells. $\lambda_{ex} = 488$ nm. (*C*) HepG2 cells were incubated with NaBu (1 mM) for 24 and 48 h and then further incubated with 5 μM HYPQG for 40 min at 37 °C, followed by fluorescence imaging. (*D*) The average fluorescence intensity found in *C*; initial signal intensity was defined as 1.0. Statistical significance *P* values (***$P < 0.001$) were determined using two-sided Student's *t* test ($n = 3$). $F/F_{control}$ represents the ratio of the fluorescence intensity of the experimental group to the control group. (*E*) Western blot was applied to monitor the change of GGT expression, as regulated by NaBu (1 mM) for 24 and 48 h in HepG2 cells. $\lambda_{ex} = 488$ nm, $\lambda_{em} = 584–676$ nm. (Scale bar, 20 μm.)

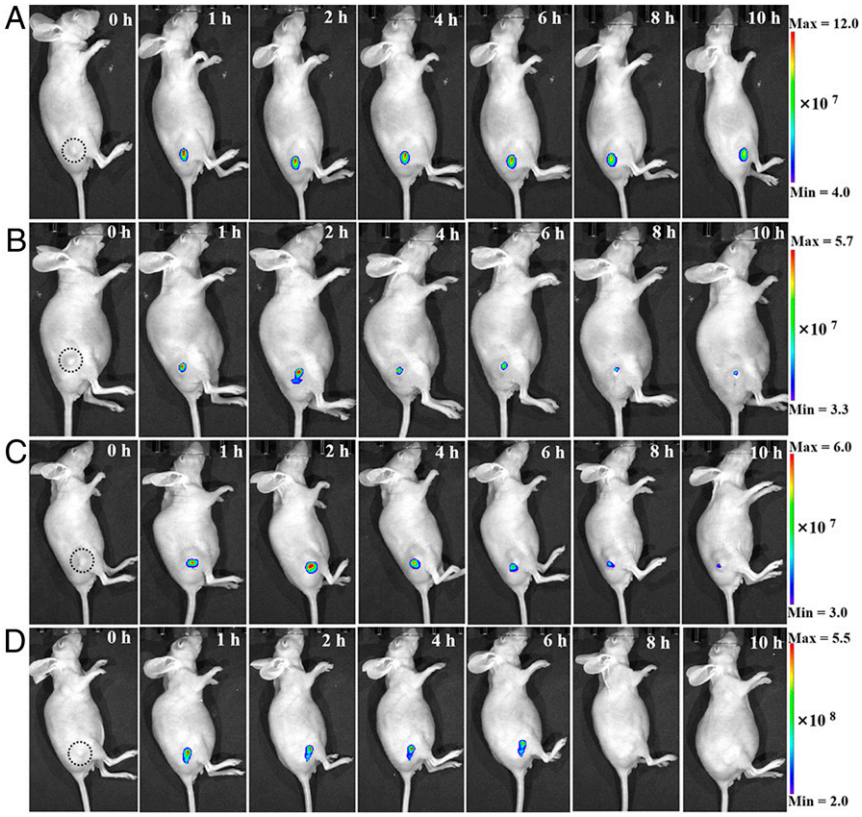

Fig. 6. Long-term in situ imaging of GGT in mouse tumors. In vivo real-time imaging of GGT in A2780-bearing nude mice after tumor injection of 20 μM HYPQG (*A*), DCMG (*B*), Bcy-GGT (*C*), and Folate-PEG5000-CY 5.5 (*D*), respectively. The quantitative analysis was displayed in *SI Appendix*, Fig. S36*A*.

expression levels of GGT. It is well known that mouse fibroblasts NIH 3T3 do not express GGT activity (39), that OVCAR3 cells express a low level of GGT, and that A2780 cells express a high level of GGT on the cell membrane (10, 40). A2780, OVCAR3, and NIH 3T3 cells were then cultured with HYPQG for 40 min, respectively, followed by carrying out fluorescence imaging. As shown in Fig. 5*A*, CLSM results demonstrated that HYPQG could be used for in situ imaging of GGT on the cell membrane for different cancer cells. The control experiment was further confirmed by flow cytometric analysis (Fig. 5*B*). Immunofluorescence and Western blot analysis also showed that GGT is a membrane-bound enzyme and that the different expression levels of GGT between A2780 and OVCRA3 cancer cells (*SI Appendix*, Figs. S33 and S34) indicated that HYPQG could be suitable for in situ imaging of GGT on cell membranes of different live cells.

Sodium butyrate (NaBu) was shown to induce cancer cell differentiation and inhibit proliferation (51). NaBu is also a well-known inducer of GGT activity on the cell membrane (52, 53). At the same time, it has been confirmed that NaBu might improve chemotherapy effect as a differentiating agent (49–52). Therefore, considering the imaging advantage of HYPQG for in situ visualization of GGT on the cell membrane, we further applied HYPQG to study the relationship between GGT activity and NaBu stimulation in HepG2 cells. As shown in Fig. 5*C*, HepG2 cells were treated with 1mM NaBu for different periods of time (0, 24, and 48 h) and then cultured with HYPQG for 40 min before fluorescence imaging. The fluorescence signal was obviously increased after pretreatment with NaBu compared with the control group in HepG2 cells (Fig. 5*D*). Western blot analysis was further utilized to confirm the fluorescence-imaging results (Fig. 5*E*). These results confirmed that the probe could be suitable for in situ imaging and monitoring change of GGT expression level on the HepG2 cell membrane.

Long-Term In Situ Imaging of GGT in Mouse Tumor. We further investigated the long-term in situ imaging ability of HYPQG in tumor-bearing mice. Initially, the fluorescence signals from the probes were all largely decreased in tumors after treatment with DON, suggesting that the enhancement of fluorescence was indeed triggered by GGT in A2780-bearing mice (*SI Appendix*, Fig. S35). After intratumor injection of HYPQG, DCMG, Bcy-GGT, and the targeted probe Folate-PEG5000-CY 5.5, respectively, the fluorescence signal was gradually enhanced and lit up the whole tumor region within 1 h (Fig. 6). The fluorescence images were acquired every 1 h, for a total of 4 h, then every 2 h for another 6 h. From 1 to 10 h after the probes were injected into the tumor, only the HYPQG probe could clearly distinguish the tumor from normal tissues compared to DCMG, Bcy-GGT, and Folate-PEG5000-CY 5.5, which suggested that the NIR precipitating fluorophore HYPQ could be used for long-term in situ imaging of the tumor region.

By virtue of fluorescence-guided surgery, cancer tissues can be illuminated and resected from the normal tissues (54, 55). However, in the process of tumor resection, traditional fluorochromes easily diffuse into adjacent tissues, potentially leading to overzealous resection and compromise of adjacent vital organs or normal tissues (56). Therefore, considering the superb performance of HYPQG in visualizing the tumor boundary accurately, it was applied to the fluorescence image-guided cancer surgery. Initially, in vitro the cancer tissue and normal muscle tissue could be obviously distinguished by in situ spraying of HYPQG (*SI Appendix*, Fig. S36 *B* and *C*). Additionally, no obvious fluorescence signal was obtained from the blank group

(*SI Appendix*, Fig. S36*D*). As shown in *SI Appendix*, Fig. S36 *E* and *F*, the tumor could be precisely lit up in situ by simply spraying HYPQG in vivo. After that, obvious fluorescent tumor tissues from the mouse were resected with a scalpel (*SI Appendix*, Fig. S36*G*). No obvious fluorescence signal was observed (*SI Appendix*, Fig. S36*H*) when the probe was sprayed again at the original site, which signified that the tumor was completely removed. Thus, our precipitating fluorochrome strategy might provide an efficient tool for long-term in situ imaging-guided surgery to realize accurate resection in the future.

Concluding Remarks

In summary, we proposed a de novo strategy to construct an antidiffusion probe by designing and screening out a precipitating fluorochrome. The strong hydrophobicity and low lipophilicity of this fluorochrome allowed it to precipitate at the reaction sites and antidiffuse into the cells, followed by the emission of strong far-red to NIR solid-state fluorescence, thereby realizing long-term in situ bioimaging on the cell membrane. As proof-of-concept, we have developed a far-red to NIR antidiffusion fluorescent probe HYPQG for the imaging of GGT activity on the cell membrane. Consequently, long-term in situ imaging of GGT on the cell membrane has been successfully realized. Moreover, HYPQG showed outstanding antidiffusion ability and signal stability compared to the commercially available dyes or probes like Memb-Tracker Red and AMCG, which have been regarded as the gold standard for realizing long-term in situ bioimaging. In addition, we applied HYPQG to achieve in situ imaging of GGT on the membrane surface of three kinds of cancer cells with different expression levels of GGT. After stimulating HepG2 cells with NaBu, the probe demonstrated its capacity for imaging and monitoring changes in GGT expression on cell membranes. By virtue of the photostable and antidiffusion characteristics, long-term in situ imaging on the cell membrane and tumor region were also successfully realized, making this probe an ideal alternative for constructing universal antidiffusion fluorescent probes, as well as providing an efficient tool for long-term in situ imaging-guided surgery in the future.

Materials and Methods

Full experimental materials and procedures for the synthesis of compounds, molecular structures, spectroscopic characterization, cellular imaging, in vivo imaging, and immunofluorescence assays are described in *SI Appendix*.

Data Availability. Supplementary crystallographic data have been deposited in The Cambridge Crystallographic Data Centre (CCDC) (HPQ [CCDC: 2045408] and HPQ4 [CCDC: 2045423]). These data can be obtained free of charge via http://www.ccdc.cam.ac.uk/data_request/cif, by emailing data_request@ccdc.cam.ac.uk, or by contacting The Cambridge Crystallographic Data Centre, 12 Union Road, Cambridge CB2 1EZ, UK; fax: +44 1223 336033. The data have been stored in Figshare (DOI: 10.6084/m9.figshare.13697521 or https://figshare.com/s/73a936fb951255d7b45d).

ACKNOWLEDGMENTS. This work was supported by the National Key R&D Program of China (Grant 2019YFA0210100 [to X.-B.Z.]), the National Natural Science Foundation of China (Grants 21977027 [to S.H.], 21890744 [to X.-B.Z.], 22074036 [to L.Y.], and 21804068 [to L.C.]), and the National Postdoctoral Program for Innovative Talents (Grant BX20190110 [to T.-B.R.]). K.L. was also supported by the Hunan Provincial Innovation Foundation for Postgraduate (Grant CX2018B189).

1. M. Riggi *et al*., Decrease in plasma membrane tension triggers PtdIns(4,5)P_2 phase separation to inactivate TORC2. *Nat. Cell Biol.* **20**, 1043–1051 (2018).
2. C. Jin *et al*., Phosphorylated lipid-conjugated oligonucleotide selectively anchors on cell membranes with high alkaline phosphatase expression. *Nat. Commun.* **10**, 2704 (2019).
3. G. Enkavi, M. Javanainen, W. Kulig, T. Róg, I. Vattulainen, Multiscale simulations of biological membranes: The challenge to understand biological phenomena in a living substance. *Chem. Rev.* **119**, 5607–5774 (2019).
4. L. Li, X. Shen, Q. H. Xu, S. Q. Yao, A switchable two-photon membrane tracer capable of imaging membrane-associated protein tyrosine phosphatase activities. *Angew. Chem. Int. Ed. Engl.* **52**, 424–428 (2013).
5. J. Mu *et al*., A small-molecule FRET reporter for the real-time visualization of cell-surface proteolytic enzyme functions. *Angew. Chem. Int. Ed. Engl.* **53**, 14357–14362 (2014).
6. M. Niwa, T. Hirayama, I. Oomoto, D. O. Wang, H. Nagasawa, Fe (II) ion release during endocytotic uptake of iron visualized by a membrane-anchoring Fe (II) fluorescent probe. *ACS Chem. Biol.* **13**, 1853–1861 (2018).
7. A. Colom *et al*., A fluorescent membrane tension probe. *Nat. Chem.* **10**, 1118–1125 (2018).
8. M. M. Ali *et al*., Cell-surface sensors: Lighting the cellular environment. *Wiley Interdiscip. Rev. Nanomed. Nanobiotechnol.* **4**, 547–561 (2012).
9. S. Xu *et al*., A cell membrane-anchored fluorescent probe for monitoring carbon monoxide release from living cells. *Chem. Sci. (Camb.)* **10**, 320–325 (2018).
10. Y. Urano *et al*., Rapid cancer detection by topically spraying a γ-glutamyltranspeptidase-activated fluorescent probe. *Sci. Transl. Med.* **3**, 110ra119 (2011).
11. X. Wu, W. Shi, X. Li, H. Ma, Recognition moieties of small molecular fluorescent probes for bioimaging of enzymes. *Acc. Chem. Res.* **52**, 1892–1904 (2019).
12. L. Shi *et al*., Rapid and ultrasensitive imaging of plasma membrane with AIE-based probe in bio-systems. *Angew. Chem. Int. Ed.* **59**, 9962–9966 (2019).
13. D. I. Danylchuk, S. Moon, K. Xu, A. S. Klymchenko, Switchable solvatochromic probes for live-cell super-resolution imaging of plasma membrane organization. *Angew. Chem. Int. Ed. Engl.* **58**, 14920–14924 (2019).
14. X. Zhang, C. Wang, L. Jin, Z. Han, Y. Xiao, Photostable bipolar fluorescent probe for video tracking plasma membranes related cellular processes. *ACS Appl. Mater. Interfaces* **6**, 12372–12379 (2014).
15. W. Xu, Z. Zeng, J. H. Jiang, Y. T. Chang, L. Yuan, Discerning the chemistry in individual organelles with small-molecule fluorescent probes. *Angew. Chem. Int. Ed. Engl.* **55**, 13658–13699 (2016).
16. H. Y. Wang *et al*., Imaging plasma membranes without cellular internalization: Multisite membrane anchoring reagents based on glycol chitosan derivatives. *J. Mater. Chem. B Mater. Biol. Med.* **3**, 6165–6173 (2015).
17. H. W. Liu *et al*., In situ localization of enzyme activity in live cells by a molecular probe releasing a precipitating fluorochrome. *Angew. Chem. Int. Ed. Engl.* **56**, 11788–11792 (2017).
18. K. Li *et al*., In situ imaging of furin activity with a highly stable probe by releasing of precipitating fluorochrome. *Anal. Chem.* **90**, 11680–11687 (2018).
19. C. Grimm *et al*., Association of gamma-glutamyltransferase with severity of disease at diagnosis and prognosis of ovarian cancer. *Br. J. Cancer* **109**, 610–614 (2013).
20. W. Zhang *et al*., Glutaminolysis is essential for energy production and ion transport in human corneal endothelium. *EBioMedicine* **16**, 292–301 (2017).
21. A. Pompella, V. De Tata, A. Paolicchi, F. Zunino, Expression of γ-glutamyltransferase in cancer cells and its significance in drug resistance. *Biochem. Pharmacol.* **71**, 231–238 (2006).
22. I. M. Mikkelsen, B. Mortensen, Y. Laperche, N. E. Huseby, The expression of γ-glutamyltransferase in rat colon carcinoma cells is distinctly regulated during differentiation and oxidative stress. *Mol. Cell. Biochem.* **232**, 87–95 (2002).
23. C. Schäfer *et al*., Gamma-glutamyl transferase expression in higher-grade astrocytic glioma. *Acta Oncol.* **40**, 529–535 (2001).
24. T. B. Ren *et al*., Harvesting hydrogen bond network: Enhance the anti-solvatochromic two-photon fluorescence for cirrhosis imaging. *Angew. Chem. Int. Ed.* **57**, 7473–7477 (2018).
25. T. B. Ren *et al*., A general method to increase Stokes shift by introducing alternating vibronic structures. *J. Am. Chem. Soc.* **140**, 7716–7722 (2018).
26. Q. Xiang *et al*., Stable olympicenyl radicals and their π-dimers. *J. Am. Chem. Soc.* **142**, 11022–11031 (2020).
27. K. Okino, S. Hira, Y. Inoue, D. Sakamaki, S. Seki, The divergent dimerization behavior of n-substituted dicyanomethyl radicals: Dynamically stabilized versus stable radicals. *Angew. Chem. Int. Ed. Engl.* **56**, 16597–16601 (2017).
28. X. B. Zhang, M. Waibel, J. Hasserodt, An autoimmolative spacer allows first-time incorporation of a unique solid-state fluorophore into a detection probe for acyl hydrolases. *Chemistry* **16**, 792–795 (2010).
29. M. Prost, L. Canaple, J. Samarut, J. Hasserodt, Tagging live cells that express specific peptidase activity with solid-state fluorescence. *ChemBioChem* **15**, 1413–1417 (2014).
30. R. Yang, S. G. Schulman, Extraordinary hyperconjugation of the methyl group in the S(1) state of 8-methylquinoline. *Luminescence* **16**, 129–133 (2001).
31. E. Kim, Y. Lee, S. Lee, S. B. Park, Discovery, understanding, and bioapplication of organic fluorophore: A case study with an indolizine-based novel fluorophore, SeoulFluor. *Acc. Chem. Res.* **48**, 538–547 (2015).
32. Y. Xu *et al*., Highly stable and multifunctional Aza-BODIPY-based phototherapeutic agent for anticancer treatment. *ACS Appl. Mater. Interfaces* **10**, 44324–44335 (2018).
33. S. P. Anthony, Polymorph-dependent solid-state fluorescence and selective metal-ion-sensor properties of 2-(2-hydroxyphenyl)-4(3H)-quinazolinone. *Chem. Asian J.* **7**, 374–379 (2012).
34. X. Wu *et al*., In vivo and in situ tracking cancer chemotherapy by highly photostable NIR fluorescent theranostic prodrug. *J. Am. Chem. Soc.* **136**, 3579–3588 (2014).
35. A. Shao *et al*., Insight into aggregation-induced emission characteristics of red-emissive quinoline-malononitrile by cell tracking and real-time trypsin detection. *Chem. Sci. (Camb.)* **5**, 1383–1389 (2014).
36. W. Fu *et al*., Rational design of near-infrared aggregation-induced-emission-active probes: In situ mapping of amyloid-β plaques with ultrasensitivity and high-fidelity. *J. Am. Chem. Soc.* **141**, 3171–3177 (2019).

37. N. Cayot, C. Lafarge, E. Bou-Maroun, P. Cayot, Substitution of carcinogenic solvent dichloromethane for the extraction of volatile compounds in a fat-free model food system. *J. Chromatogr. A* **1456**, 77–88 (2016).
38. I. Stefanov, B. Vlaeminck, V. Fievez, A novel procedure for routine milk fat extraction based on dichloromethane. *J. Food Compos. Anal.* **23**, 852–855 (2010).
39. M. H. Hanigan, W. A. Ricketts, Extracellular glutathione is a source of cysteine for cells that express gamma-glutamyl transpeptidase. *Biochemistry* **32**, 6302–6306 (1993).
40. X. Hou, F. Zeng, S. Wu, A fluorescent assay for γ-glutamyltranspeptidase via aggregation induced emission and its applications in real samples. *Biosens. Bioelectron.* **85**, 317–323 (2016).
41. F. Wang *et al*., Fluorescent in situ targeting probes for rapid imaging of ovarian-cancer-specific gamma-glutamyl transpeptidase. *Angew. Chem. Int. Ed. Engl.* **54**, 7349–7353 (2015).
42. S. Park *et al*., Indocyanine-based activatable fluorescence turn-on probe for γ-glutamyl transpeptidase and its application to the mouse model of colon cancer. *ACS Sens.* **1**, 579–583 (2016).
43. L. Li *et al*., Monitoring γ-glutamyl transpeptidase activity and evaluating its inhibitors by a water-soluble near-infrared fluorescent probe. *Biosens. Bioelectron.* **81**, 395–400 (2016).
44. L. Li, W. Shi, Z. Wang, Q. Gong, H. Ma, Sensitive fluorescence probe with long analytical wavelengths for γ-glutamyl transpeptidase detection in human serum and living cells. *Anal. Chem.* **87**, 8353–8359 (2015).
45. R. J. Iwatate *et al*., Silicon rhodamine-based near-infrared fluorescent probe for gamma-glutamyl transferase. *Bioconjug. Chem.* **29**, 241–244 (2018).
46. Z. Luo *et al*., Targeted delivery of a gamma-glutamyl transpeptidase activatable near-infrared-fluorescent probe for selective cancer imaging. *Anal. Chem.* **90**, 2875–2883 (2018).
47. P. Zhang *et al*., A two-photon fluorescent sensor revealing drug-induced liver injury via tracking γ-glutamyltranspeptidase (GGT) level in vivo. *Biomaterials* **80**, 46–56 (2016).
48. J. Ou-Yang *et al*., Detecting and imaging of γ-glutamyl transpeptidase activity in serum, live cells, and pathological tissues with a high signal-stability probe by releasing a precipitating fluorochrome. *ACS Sens.* **3**, 1354–1361 (2018).
49. Y. Chen *et al*., A molecular-logic gate for COX-2 and NAT based on conformational and structural changes: Visualizing the progression of liver disease. *Chem. Sci. (Camb.)* **11**, 6209–6216 (2020).
50. W. Li *et al*., Achieving the ratiometric imaging of steroid sulfatase in living cells and tissues with a two-photon fluorescent probe. *Chem. Commun. (Camb.)* **56**, 1349–1352 (2020).
51. L. Wasserman, J. Nordenberg, E. Beery, A. A. Deutsch, A. Novogrodsky, Differential effects of sodium butyrate and dimethylsulfoxide on gamma-glutamyl transpeptidase and alkaline phosphatase activities in MCF-7 breast cancer cells. *Exp. Cell Biol.* **55**, 188–193 (1987).
52. J. Wu, Y. Cheng, B. A. Jönsson, A. Nilsson, R. D. Duan, Acid sphingomyelinase is induced by butyrate but does not initiate the anticancer effect of butyrate in HT29 and HepG2 cells. *J. Lipid Res.* **46**, 1944–1952 (2005).
53. H. G. Wang *et al*., Anticancer effects of sodium butyrate on hepatocellular carcinoma cells in vitro. *Int. J. Mol. Med.* **31**, 967–974 (2013).
54. M. J. Landau, D. J. Gould, K. M. Patel, Advances in fluorescent-image guided surgery. *Ann. Transl. Med.* **4**, 392 (2016).
55. R. R. Zhang *et al*., Beyond the margins: Real-time detection of cancer using targeted fluorophores. *Nat. Rev. Clin. Oncol.* **14**, 347–364 (2017).
56. L. Wasserman *et al*., Sodium butyrate enhances the activities of membranal enzymes and increases drug sensitivity in a cell line from ascitic fluid of an ovarian carcinoma patient. *Eur. J. Cancer Clin. Oncol.* **25**, 1765–1768 (1989).